

Scaling Radar Measurements for Advanced Algorithms

Steven H.R. Brady and Michael A. Saville

Department of Electrical and Computer Engineering, Air Force Institute of Technology,

Wright-Patterson AFB, OH, 45433 USA

e-mail: michael.saville@afit.edu., steven.brady@afit.edu

Abstract—This paper describes waveform diverse signal measurements using a two channel laboratory radar system. Using a combination of a Lab-Volt™ radar training system, Tektronix™ arbitrary waveform generator (AWG), Tektronix™ digital oscilloscope (DSO), and Tektronix™ real-time spectrum analyzer (RSA), a two channel, waveform diverse, multiple-input, multiple-output (MIMO) system is configured to collect both MIMO and bistatic radar measurements. In the experiments, the radar operates at X-band and samples the echoes at radio frequency (RF) before down-conversion into in-phase and quadrature (I/Q) channels. The laboratory environment does not need any special treatment as an anechoic chamber because the system uses very short duration and low power waveforms. Measured data for the MIMO radar is presented along with discussion of the bistatic configuration.

Index Terms—bistatic radar, point target measurement, multistatic ambiguity function.

I. INTRODUCTION

Although it is generally agreed that waveform diversity improves some aspects of radar performance, there are relatively few publicly available studies that demonstrate improved performance in practical systems. Waveform diversity has been applied to radar systems and radar signal processing since the 1930s, but it has only existed as a separate research area since the 1990s [1]. Examples of waveform diversity research under different guises include radio frequency tomography (RFT); multiple-input, multiple-output (MIMO) radar; and, frequency diverse array (FDA) radar. Amongst other technological advances, waveform diversity is anticipated to be a key enabling technology in future distributed-aperture and layered sensing systems [2].

Theoretically-based waveform diversity research suggests that in many cases waveform diversity improves radar system performance; however, the analytic models used to support the results often neglect practical considerations. This is highlighted in [3] where the authors compare theoretical MIMO radar to phased array radar performance with respect to performance, complexity and cost. The lack of practical performance considerations in academic research may be partly due to the prohibitive cost and difficulty associated with measuring radar signals produced by advanced configurations.

In this paper, we present waveform diversity experiments using a scaled, reconfigurable, X-band radar system at the Radar Instrumentation Laboratory (RAIL), Air Force Institute of Technology (AFIT). RAIL is equipped with a reconfigurable

Lab-Volt™ Radar Training System (LVRTS) and Tektronix™ Microwave Measurement Suite which features a 10GSa/s AWG, a 40GSa/s DSO, and a 13GHz RSA. Researchers have unrestricted access to the facility without the overhead of operating a radar range or anechoic chamber because the radiated power produced by the equipment is significantly below safe exposure limits.

The X-band radar system, inclusive of the target area, occupies an area of approximately $3m \times 4m$ and clutter due to the laboratory environment is minimized by using short-duration, low-power signals. Compared to a traditional radar test configuration, the target area, signal power and signal duration are scaled down while the signal bandwidth, component cost and instrument costs are proportionally scaled up. We expect that the approach will allow AFIT students and researchers to validate their simulation results using measured data. In the remainder of the paper we describe how we configured the system, and how we have used the system to support waveform diversity research.

II. EXPERIMENTAL CONFIGURATIONS

The instruments and circuits used for a two-channel radar are shown in Figure 1 and the geometries describing the experiments are shown in Figure 2. The instruments communicate with each other through a local area network (LAN) and they were controlled using a MATLAB® script hosted on the DSO. The LVRTS's voltage controlled oscillator (VCO) generates the local oscillator (LO) waveform, with frequency $\omega_0 \approx 2\pi(9.8 \times 10^9)$, to the pre-conditioning circuit (PCC) while the RSA continuously estimates the VCO's fundamental frequency, $\hat{\omega}_0$.

The PCC is shown in Figure 3(a), and it approximates a high-speed, radio frequency (RF) switch. The purpose of the PCC is to improve the system's sensitivity to small targets by reducing the amplitude of the out-of-pulse LO waveform that leaks through the non-ideal circuit components and reaches the digital receiver front-end (dRFE). The PCC multiplies the LO waveform with rectangular pulses generated by the AWG and outputs a rectangular, RF pulse. In addition to generating the two rectangular pulses used by the PCC, the AWG generates two baseband transmit signals $\tilde{s}_p(t)$, and a synchronization pulse to trigger the DSO.

Two identical, transmit-receive circuits (TRCs), each with a simplified circuit diagram shown in Figure 3(b), multiply the

Report Documentation Page			Form Approved OMB No. 0704-0188	
<p>Public reporting burden for the collection of information is estimated to average 1 hour per response, including the time for reviewing instructions, searching existing data sources, gathering and maintaining the data needed, and completing and reviewing the collection of information. Send comments regarding this burden estimate or any other aspect of this collection of information, including suggestions for reducing this burden, to Washington Headquarters Services, Directorate for Information Operations and Reports, 1215 Jefferson Davis Highway, Suite 1204, Arlington VA 22202-4302. Respondents should be aware that notwithstanding any other provision of law, no person shall be subject to a penalty for failing to comply with a collection of information if it does not display a currently valid OMB control number.</p>				
1. REPORT DATE MAY 2010	2. REPORT TYPE	3. DATES COVERED 00-00-2010 to 00-00-2010		
4. TITLE AND SUBTITLE Scaling Radar Measurements for Advanced Algorithms			5a. CONTRACT NUMBER	
			5b. GRANT NUMBER	
			5c. PROGRAM ELEMENT NUMBER	
6. AUTHOR(S)			5d. PROJECT NUMBER	
			5e. TASK NUMBER	
			5f. WORK UNIT NUMBER	
7. PERFORMING ORGANIZATION NAME(S) AND ADDRESS(ES) Air Force Institute of Technology, Department of Electrical and Computer Engineering, Wright-Patterson AFB, OH, 45433			8. PERFORMING ORGANIZATION REPORT NUMBER	
9. SPONSORING/MONITORING AGENCY NAME(S) AND ADDRESS(ES)			10. SPONSOR/MONITOR'S ACRONYM(S)	
			11. SPONSOR/MONITOR'S REPORT NUMBER(S)	
12. DISTRIBUTION/AVAILABILITY STATEMENT Approved for public release; distribution unlimited				
13. SUPPLEMENTARY NOTES See also ADM002322. Presented at the 2010 IEEE International Radar Conference (9th) Held in Arlington, Virginia on 10-14 May 2010. Sponsored in part by the Navy.				
14. ABSTRACT This paper describes waveform diverse signal measurements using a two channel laboratory radar system. Using a combination of a Lab-Volt™ radar training system, Tektronix™ arbitrary waveform generator (AWG), Tektronix™ digital oscilloscope (DSO), and Tektronix™ real-time spectrum analyzer (RSA), a two channel, waveform diverse, multiple-input,multipleoutput (MIMO) system is configured to collect both MIMO and bistatic radar measurements. In the experiments, the radar operates at X-band and samples the echoes at radio frequency (RF) before down-conversion into in-phase and quadrature (I/Q) channels. The laboratory environment does not need any special treatment as an anechoic chamber because the system uses very short duration and low power waveforms. Measured data for the MIMO radar is presented along with discussion of the bistatic configuration.				
15. SUBJECT TERMS				
16. SECURITY CLASSIFICATION OF:			17. LIMITATION OF ABSTRACT Same as Report (SAR)	18. NUMBER OF PAGES 6
a. REPORT unclassified	b. ABSTRACT unclassified	c. THIS PAGE unclassified	19a. NAME OF RESPONSIBLE PERSON	

rectangular RF pulse with a baseband waveform diverse signal, $\tilde{s}_p(t)$, to produce the RF transmit signal $s_p(t)$. The signals are transmitted into a 1m^2 target area and the signals of interest are collected by the receive antennas. The waveform passing through the TRC's circulators are sampled directly at RF by the DSO. The dRFE, implemented using MATLAB® code, converts the signals into baseband I/Q signals.

We used the two channel radar with the aim of validating a phase-code, frequency and chirp diverse signal model in two related experiments. In the first experiment we measured the aggregate far-field transmit signal produced by the system when it transmits combinations of phase-coded (PC), single sub-carrier (SC), multiple sub-carrier (MC) and linear frequency modulated (LFM) signals. In the second experiment we measured signals collected by the two transmit antennas due to the transmit signals scattered from two targets in the far-field using the set of SC, MC and LFM signals.

In the third experiment we reconfigured the system to emulate a tomographic configuration. A single antenna was used to illuminate a small metal sphere at the center of an imaginary circle while a single antenna was placed at points on the circle's circumference to measure the bistatic scattering from the target. The data collected during the experiment was used to validate simulated multistatic ambiguity function (MAF) experiments and the results are presented in an accompanying paper [4].

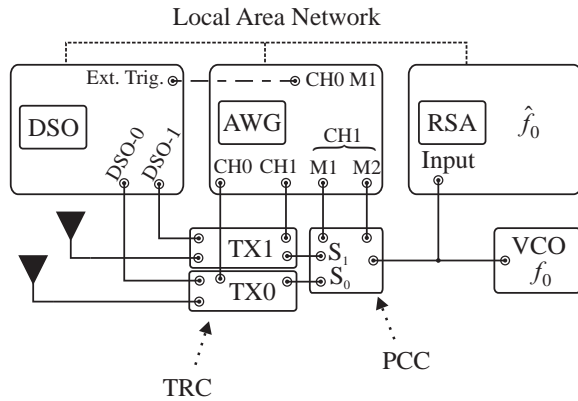


Fig. 1. Connection block diagram for the AWG, DSO and RSA. The instruments are controlled using MATLAB® code hosted on the DSO and the instruments communicate through a LAN. The code initializes each of the instruments for a particular experimental geometry and schedules a number of trials for each signal permutation. For each trial the code configures the two AWG transmit waveforms, stores the samples collected by the DSO, and obtains an estimate of the LO frequency using the RSA.

A. Experiment 1 - transmit signal measurements

We had complementary objectives for the first experiment. First, we aimed to build a reconfigurable two-channel waveform diverse radar system that could be used to generate and measure waveform diverse radar signals. Second, we aimed to confirm whether our signal model predicts the aggregate signal in the far-field with at least fair agreement. The geometry for the experiment is shown in Figure 2, and the experiment used $P = 2$ 2-inch, horn antennas aligned to the \hat{y} -axis and centered

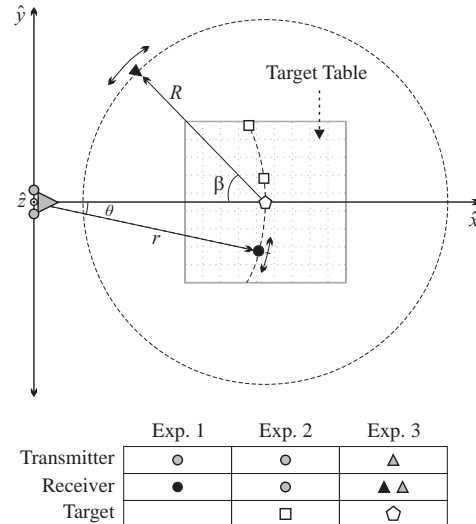


Fig. 2. Geometry for the three experiments. Experiment 1 used a 4-inch, standard gain, horn antenna to measure the signal transmitted from two, 2-inch horn antennas in a linear array configuration. Experiment 2 measured the signals collected by the two antennas, configured as in Experiment 1, due to scattering from two, 4-inch, square, metal plates. Experiment 3 measured the signal scattered from a 1-inch metal sphere which was illuminated by a parabolic dish antenna located at the origin. A 4-inch pyramidal horn antenna was used to measure the scattered signal around a circle with constant radius R and with a bistatic angle between transmitter and receiver of β .

about the origin, while a 4-inch, horn antenna was used to measure the transmit signal.

The displacement of the p th antenna is

$$\bar{\mathbf{d}}_p = \hat{\mathbf{y}} \Delta d_{\hat{y},t} \left(p - \frac{P-1}{2} \right), \quad (1)$$

and the transmit antennas are separated by $\Delta d_{\hat{y},t} = 0.055\text{m}$. For the radar's LO frequency, the electrical separation between antennas is $\Delta d_{\hat{y},t} \approx 2\lambda_0$ and we expected angular aliasing of the far-field transmit signal.

We used the AWG to generate the baseband PC, SC, MC and LFM signals, where the p th baseband signal is

$$\begin{aligned} \tilde{s}_p(t) = & \sum_{b=0}^{B-1} \sum_{m=0}^{M-1} \sum_{n=0}^{N-1} A_{p,b,m,n} \hat{b} \left(\frac{t - mT_c - nT_p}{T_c} \right) \\ & \times \exp(j\varphi_{p,b,m,n}) \exp[j\Delta\omega_b(t - mT_c - nT_p)] \\ & \times \exp[j\pi\vartheta_{p,b,m,n}(t - mT_c - nT_p)^2]. \end{aligned} \quad (2)$$

The coherent processing interval (CPI) has N pulses with pulse repetition interval (PRI) T_p . Within each pulse there are BM temporal-spectral chips with: amplitude A , phase φ , LFM rate ϑ , frequency offset $\Delta\omega_b$, and duration T_c . The set of characteristic parameters for each temporal-spectral chip is $\tilde{\Upsilon} = (A, \varphi, \vartheta)$. The pulse shape function $\hat{b}(t)$ is a unit-amplitude, shifted rectangular function given by

$$\hat{b}(t) = \begin{cases} 1, & 0 < t \leq 1 \\ 0, & \text{else.} \end{cases} \quad (3)$$

We found that the AWG could reproduce theoretical waveforms, providing the maximum of either the sub-carrier frequency or the LFM signal's instantaneous frequency is less than approximately 1GHz.

We used the 4-inch, horn antenna to measure the transmit signal at 21 locations between azimuth angles $\theta \in \pm 23.5^\circ$ at a constant range $r_q = 1.1\text{m}$. Once we developed a robust method to digitally I/Q demodulate the received signals we found that the system was highly coherent, and that by sampling the transmit signal over time we could emulate $Q = 21$ identical antennas receiving the transmit signal simultaneously.

The displacement of the q th antenna is

$$\bar{\mathbf{d}}_q = r_q [\hat{\mathbf{x}} \cos(\arcsin u_q) + \hat{\mathbf{y}} u_q], \quad (4)$$

where $u_q = \sin \theta_q = 0.04q - 0.4$ and θ_q is the azimuth angle. The signal at the q th antenna, simplified using the far-field and narrowband array approximations to the propagation delay, is

$$s(t, \bar{\mathbf{d}}_q) = K_{tx} \sum_{p=0}^{P-1} \exp[j\omega_0(t - \tau_0 + \Delta\tau_p)] \times \tilde{s}_p(t - \tau_0 + \Delta\tau_p). \quad (5)$$

The propagation delay from the origin to any point at a range r_q is $\tau_0 = r_q/c$ where c is the speed of light. The differential propagation delay from the p th transmitter to the origin in the direction of the q th receiver is $\Delta\tau_p = |\bar{\mathbf{d}}_p|u_q/c$. The notation $|\cdot|$ represents the magnitude of a geometric vector. The amplitude scaling term K_{tx} can be included to account for amplitude scaling predicted by the Friis transmission equation, but, is neglected because the transmit antennas were identical and the comparative results were normalized to have unit amplitude.

We designed several classes of baseband signals which the AWG could generate. The first set of signals were monochromatic, binary, PC signals with $M = 4$ and $T_c = 500\text{ps}$. The set of PC signals included the four 4-chip, Hadamard sequences and the two 4-chip, Barker sequences. These codes were of interest because the mutually orthogonal Hadamard sequences are found frequently in the literature while the Barker sequences have the desirable, minimum autocorrelation sidelobes.

The model for the PC signals reduces to

$$\tilde{s}_p^{(PC)}(t) = \sum_{m=0}^{M-1} \sum_{n=0}^{N-1} A_{p,m,n} \hat{b} \left(\frac{t - mT_c - nT_p}{T_c} \right) \times \exp(j\varphi_{p,m,n}). \quad (6)$$

The phase code transmitted from the p th antenna will be described using a vector of phases where $\tilde{\varphi}_p = (\varphi_{p,0,n}, \dots, \varphi_{p,M-1,n})$ and the m th vector element is referenced by $\tilde{\varphi}_{p,m}$.

The second set of waveforms we designed for the AWG included four different single-chip SC, MC, and LFM signals – a total of twelve waveforms. We both simulated and measured data for every permutation of choosing two signals from the complete set of signals, and each permutation was transmitted

from the antennas in separate trials. Setting the chip index to $M = 1$ the model's notation simplifies slightly to

$$\begin{aligned} \tilde{s}_p(t) &= \sum_{b=0}^{B-1} \sum_{n=0}^{N-1} A_{p,b,n} \hat{b} \left(\frac{t - nT_p}{T_c} \right) \\ &\times \exp(j\varphi_{p,b,n}) \exp[j\Delta\omega_b(t - nT_p)] \\ &\times \exp[j\pi\vartheta_{p,b,n}(t - nT_p)^2]. \end{aligned} \quad (7)$$

The single chip waveforms were designed with: constant amplitude $A = 1$, equally spaced, orthogonal frequency offsets $\Delta\omega_b = 2\pi(200 \times 10^6)b$, equal chip duration $T_c = 5\text{ns}$, and equal magnitude LFM rates $|\vartheta| = 400 \times 10^6/T_c$. The signal configurations used for the comparative results will be stated explicitly in Section III.

B. Experiment 2 - received signal measurements

Once we evaluated transmit signal model predictions, we turned our attention to whether the model could predict signals received by the two 2-inch antennas. We placed two 4-inch, square, metal plates on the Lab Volt system's target table at an equal far-field range but, separated in azimuth angle. The experiment's geometry is shown in Figure 2, and the model's receiver locations are re-defined from the previous experiment such that $Q = 2$, the receivers are co-located with the transmitters $\bar{\mathbf{d}}_q = \bar{\mathbf{d}}_p$, and the indices are equal $q = p$.

The $P = 2$ transmit signals propagate to the $I = 2$ targets. The i th target has parameters $\Xi_i = (r_i, u_i, v_i)$ where r_i is the target's range, $u_i = \sin \theta_i$ is the target's angular parameter, and v_i is the target's velocity relative to the radar. The parameters for the two targets were

$$\Xi_0 = (1.1\text{m}, 0.12, 0) \text{ and } \Xi_1 = (1.1\text{m}, 0.4, 0), \quad (8)$$

and we modeled the targets as ideal point targets for convenience.

Incorporating two-way propagation delays, which are simplified using the far-field and narrowband array approximations to the propagation delays, the signal scattered from the targets and collected by the q th antenna is proportional to

$$r_q(t) = \sum_{i=0}^{I-1} K_{tx,rx,i} \exp[j\omega_0(t - 2\tau_{0,i})] \tilde{s}_q(t, \Xi_i) + n_q(t), \quad (9)$$

where $K_{tx,rx,i}$ is the amplitude scaling predicted by the range equation, $n_q(t)$ is the receiver noise, $\tau_{0,i} = r_i/c$ is the one-way propagation delay from the origin to the i th target and

$$\begin{aligned} \tilde{s}_q(t, \Xi_i) &= \sum_{p=0}^{P-1} \exp[j\omega_0(\Delta\tau_{p,i} + \Delta\tau_{q,i})] \\ &\times \tilde{s}_p(t - 2\tau_0 + \Delta\tau_{p,i} + \Delta\tau_{q,i}), \end{aligned} \quad (10)$$

is the ideal, baseband signal received from the i th target. The amplitude scaling $K_{tx,rx,i}$ is set to unity because the targets are the same size, with their surface normals directed to the origin, and are at the same range. The differential propagation delays are now $\Delta\tau_{p,i} = |\bar{\mathbf{d}}_p|u_i/c$ and $\Delta\tau_{q,i} = |\bar{\mathbf{d}}_q|u_i/c$.

The received signals are I/Q demodulated in the dRFE resulting in complex-valued, baseband, received signals

$$x_q(t) = \exp\left[-j(\hat{\omega}_0 t + \hat{\phi})\right] r_q(t). \quad (11)$$

Recall that $\hat{\omega}_0$ is the LO frequency estimated using the RSA and $\hat{\phi}$ is an estimate of the LO's initial phase referenced to the start of the signal. For the simulated data $\hat{\omega}_0 = \omega_0$ and $\hat{\phi} = 0$.

Following the digital I/Q demodulation, we process the measured and simulated received signals using a set of correlators. The complex conjugate of the ideal signal at the q th receiver, $\tilde{s}_q^*(t, \hat{\Xi}_t)$, is correlated with the received signal. The ideal signal models the signal scattered from an ideal point target with estimated parameters $\hat{\Xi}_t = (r, u, 0)$. The sum of the Q correlator outputs is

$$\begin{aligned} y(r, u) &= \sum_{q=0}^{Q-1} \int_{-\infty}^{\infty} x_q(t) \tilde{s}_q^*(t, \hat{\Xi}_t) dt \\ &= \sum_{q=0}^{Q-1} y_q(t, \hat{\Xi}_t), \end{aligned} \quad (12)$$

which can also be expressed as a function of time related through $t = 2r/c$. Similar to the previous experiment, we measured and simulated data for every permutation of choosing two signals from the set of twelve SC, MC, and LFM signals. We processed the data using the dRFE and the correlator to produce range-angle plots and representative results are discussed in Section III.

C. Experiment 3 - tomographic measurements

For the final experiment we measured a set of bistatic received signals to support simulated MAF results. The geometry used to describe the experiment's configuration is shown in Figure 2. We modified the hardware configuration compared to the previous experiments in order to improve the receiver's sensitivity. We inserted the LVRTS's amplifier module prior to the DSO input to increase the received signal's amplitude. To operate the amplifier we also needed to use the LVRTS's synchronizer module to trigger the amplifier, DSO and AWG.

We used a parabolic dish antenna, positioned at the origin of the coordinate system and illuminated a 1-inch diameter, metal sphere with parameters $\Xi_0 = (1.02m, 0, 0)$. Given the range resolution of a signal with a 2GHz bandwidth, the sphere is a fair approximation to an ideal point target. A 4-inch horn antenna was used to collect the scattered signal and was placed at twelve points on the circumference of a circle centered on the target with radius $R = 1.02m$. The bistatic angle β describes the angle between the transmit and receive antennas with positive values of β corresponding to a clockwise increase in the bistatic angle.

Similar to Experiment 1, the system's coherency allows the separately collected signals at different locations to be combined to emulate a tomographic ring of $Q = 12$ receive antennas simultaneously collecting the signal scattered from

the target. The q receivers have bistatic angles

$$\beta_q = q \frac{\pi}{6} + \frac{\pi}{12} \quad (13)$$

and the q th receiver's displacement is

$$\bar{\mathbf{d}}_q = \hat{\mathbf{x}}(r_0 - R \cos \beta_q) + \hat{\mathbf{y}} R \sin \beta_q \quad (14)$$

where r_0 is the target's range from the origin.

The received signals can be modeled using Equations (9) and (10) provided the actual bistatic propagation delay is included. The delay $\tau_{p,0}$ is the delay from the transmitter to the target, and $\tau_{q,0}$ is the delay from the target to the receiver. In the tomographic configuration, with a single target at the center of the circle, the bistatic delays are equal for all Q receivers. We digitally demodulated the measured data using the process described in Section II-B, and the data were used in the MAF algorithm with results reported in the accompanying paper [4].

III. RESULTS

A. Experiment 1

We first compared the measured and simulated data for PC signals using the configuration and signal model described in Section II-A. It was found that a differential delay between the two transmit channels caused the transmit signal's focus to shift to $u = 0.12$. Accounting for the shift in the signal model, the simulated and measured PC data were in fair agreement for every permutation.

Figure 4 shows the measured and simulated aggregate transmit signal when the Barker sequence $\tilde{\varphi}_0^{\text{PC1}} = (0, 0, 0, \pi)$ is transmitted from the $p = 0$ antenna, and the Hadamard sequence $\tilde{\varphi}_1^{\text{PC2}} = (0, 0, 0, 0)$ is transmitted from the $p = 1$ antenna. The location of the peaks and nulls in the two patterns are approximately equal showing fair agreement. The model presented in Section II-A adequately describes monochromatic, binary, PC signals.

Next, we compare the measured and simulated data for MC signals. The signal transmitted from the $p = 0$ antenna has characteristics

$$\tilde{\Upsilon}_{0,b,n}^{\text{MC1}} = \begin{cases} (1, -b\pi, 0), & b = 0, 2 \ \forall n \\ (0, 0, 0), & \text{else}, \end{cases} \quad (15)$$

and the signal transmitted from the $p = 1$ antenna is

$$\tilde{\Upsilon}_{1,b,n}^{\text{MC2}} = \begin{cases} (1, -b\pi, 0), & b = 1, 3 \ \forall n \\ (0, 0, 0), & \text{else}. \end{cases} \quad (16)$$

Plots of the measured and simulated data are shown in Figure 5. For the SC, MC and LFM signals the model did not predict the signal transmitted by the radar. Upon further examination, the TRCs were initially built for binary, PC signal generation and are based on a double sideband (DSB) modulator design. However, the baseband signal model in Eq. (7) predicts the signal generated output from a single sideband (SSB) modulator and assumes the signals have constant envelopes.

As a consequence we modified the signal model to use the real part of the baseband signal $\text{Re}\{\tilde{s}_p(t)\}$ in Eq. (5) and recalculated the simulated data. Following the modification, the measured and simulated MC transmit signals $\tilde{\Upsilon}_{0,b,n}^{\text{MC1}}$ and $\tilde{\Upsilon}_{1,b,n}^{\text{MC2}}$, shown in Figure 6, are in fair agreement. We observed that the modified model predicts the measured data with fair agreement in all signal permutations.

Another example is provided for an SC signal transmitted from the $p = 0$ antenna with signal characteristics

$$\tilde{\Upsilon}_{0,b,n}^{\text{SC1}} = \begin{cases} (1, -b\pi, 0), & b = 3 \forall n \\ (0, 0, 0), & \text{else,} \end{cases} \quad (17)$$

and an LFM signal transmitted from the $p = 1$ antenna with signal characteristics

$$\tilde{\Upsilon}_{1,b,n}^{\text{LFM1}} = \begin{cases} (1, 0, 400 \times 10^6 / T_c), & b = 0 \forall n \\ (0, 0, 0), & \text{else.} \end{cases} \quad (18)$$

Plots of the measured and simulated far-field signals are shown in Figure 7.

In both Figures 6 and 7 the primary discrepancies are due to non-ideal waveform generation using the PCC, the TRCs and practical antennas. The first discrepancy is that the measured signal's amplitude over the first 1ns appears to be significantly diminished. This is most likely because the pulse envelope is not an ideal rectangular function. The second discrepancy is that the measured signal's null at $u = -0.2$ is appreciably wider than predicted by simulated data. Differences between the measured and the simulated data over the angular dimension are most likely due to the practical antenna beam patterns and antenna misalignments.

In summary, the experiment's result showed that we did not build the correct TRC to generate the waveform diverse transmit signals our model aimed to represent. However, given the TRC design, we were successful in predicting the transmit signal by using a modified signal model.

B. Experiment 2

Following the result from the first experiment, we modified Eq. (10) to use the real part of the baseband signal, and we used the modified signal model to simulate data for the configuration described in Section II-B. Both the simulated and the measured data were processed using the correlator in Eq. (12) to produce range-angle plots of the target scene.

The range-angle plots created from the measured and simulated data for every permutation of choosing two signals from the set of SC, MC and LFM signals were in fair agreement. We found that when a constant frequency (CF) pulse was transmitted from both antennas the correlator produced a range-angle plot whose pattern exhibited an array factor and range profile consistent with values predicted by CF array theory. This confirmed that we implemented the correlator correctly.

Figure 8 shows the range-angle plots for the received $\tilde{\Upsilon}_{0,b,n}^{\text{MC1}}$ and $\tilde{\Upsilon}_{1,b,n}^{\text{MC2}}$ MC signals scattered from the two square, metal targets. The first target, located at $u = 0.12$, has a large

mainlobe response while the response due to the second target, at $u = 0.4$, almost appears to be a sidelobe from the first target. An interesting feature seen in the plots is an apparent coupling between the range and angle which causes the range sidelobes to appear vertically skewed.

Range-angle plots for the measured and simulated received signal due to the SC signal, $\tilde{\Upsilon}_{0,b,n}^{\text{SC1}}$, and the LFM signal, $\tilde{\Upsilon}_{1,b,n}^{\text{LFM1}}$ are shown in Figure 9. The plots created using the measured and the simulated data are in fair agreement. Compared to the MC configuration, the range-angle coupling appears less severe. This may be because the SC/LFM configuration only spans half the MC configuration's bandwidth suggesting a relationship between signal bandwidth and the degree of the range-angle coupling.

In summary, the SSB signal model described in Section II-B did not predict the range-angle plots produced by the correlator using the measured data. However, when the model was modified to represent DSB signals, the range-angle plots produced using simulated data were in fair agreement to those produced using measured data.

IV. CONCLUSIONS

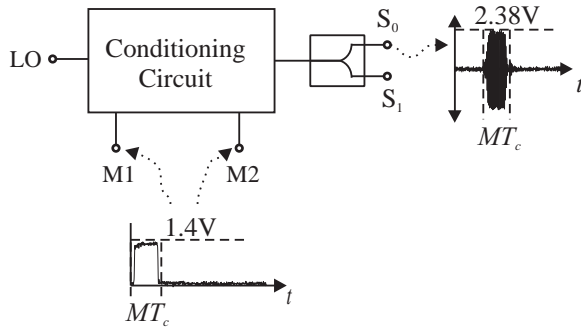
A two channel MIMO laboratory radar was used to collect static radar measurements to support waveform diversity and advanced radar signal processing research. The approach reduces the radar's physical footprint which is made possible by using short duration, low power signals. The benefit is that controlled facilities are not required to house or operate the system, but this increases the cost of acquiring high bandwidth components and fast instruments. The experimental geometries are miniaturized but could easily be scaled-up for field testing using narrow bandwidth, high power components and slower instruments. The combination of the system synchronization, the DSO's accurate high-speed sampling and the digital I/Q demodulation resulted in a highly coherent system. This allowed more complex geometries to be emulated by combining data collected during separate trials, using fewer channels. Incremental improvements to the configuration's hardware or software could be incorporated in future work.

ACKNOWLEDGMENT

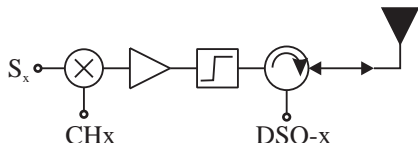
The views expressed in this paper are those of the author and do not reflect the opinions of the US or Australian governments, respective departments of defense, or the United States or Royal Australian Air Forces.

REFERENCES

- [1] M. Wicks, "A brief history of waveform diversity," in *IEEE Radar Conference*, May 2009, pp. 1–6.
- [2] M. C. Wicks and P. Antonik, "Waveform diversity in intelligent sensor systems," in *The Institution of Engineering and Technology Forum on Waveform Diversity and Design in Communications, Radar and Sonar*, Nov. 2006, pp. 1–6.
- [3] F. Daum and J. Huang, "Mimo radar: Snake oil or good idea?" *IEEE Aerospace and Electronic Systems Magazine*, vol. 24, no. 5, pp. 8–12, May 2009.
- [4] I. Bradaric, G. Capraro, S. Brady, M. Saville, and M. Wicks, "Multistatic measurements in a controlled laboratory environment," in *IEEE International Radar Conference 2010*, Washington DC, USA, May 2010.

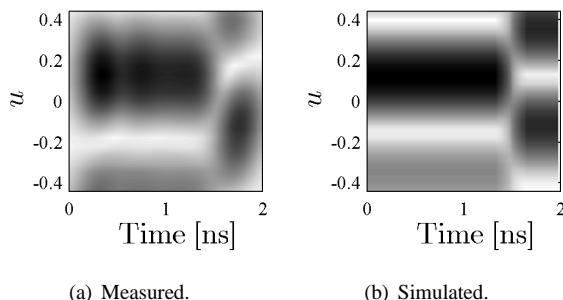


(a) Signal conditioning circuit block diagram.



(b) Transmit-receive simplified circuit diagram.

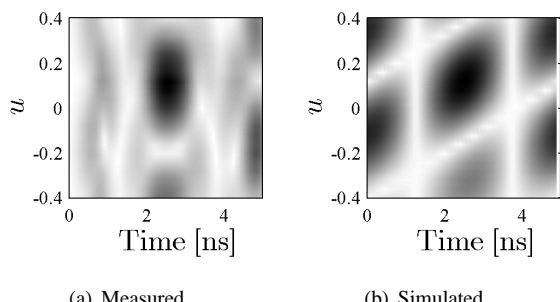
Fig. 3. Simplified diagrams of: (a) the PCC and (b) the TRC. The PCC increases the receiver's sensitivity by reducing the amount of out-of-pulse LO signal that leaks through non-ideal components to the dRFE. The TRC implements a product modulator resulting in a DSB transmit waveform. The waveform at the output of the TRC's circulator is sampled by the DSO and stored for post-processing.



(a) Measured.

(b) Simulated.

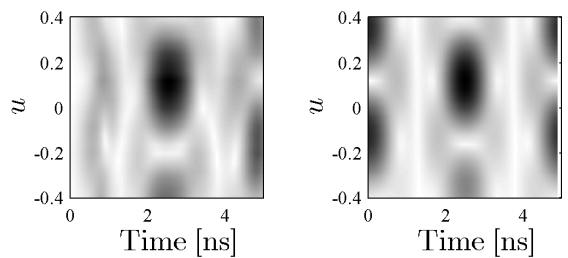
Fig. 4. Measured (a) and simulated (b) transmit signals for the Barker sequence $\tilde{\varphi}_0^{\text{PC}1}$, and the Hadamard sequence $\tilde{\varphi}_1^{\text{PC}2}$. The measured and simulated transmit signals are in fair agreement.



(a) Measured.

(b) Simulated.

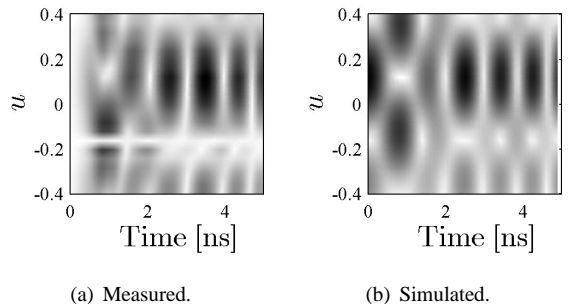
Fig. 5. Measured (a) and simulated (b) transmit signals for the MC signals $\tilde{Y}_{0,b,n}^{\text{MC}1}$ and $\tilde{Y}_{1,b,n}^{\text{MC}2}$. The measured and simulated transmit signals do not agree because the model does not adequately represent the signals output by the TRCs.



(a) Measured.

(b) Simulated.

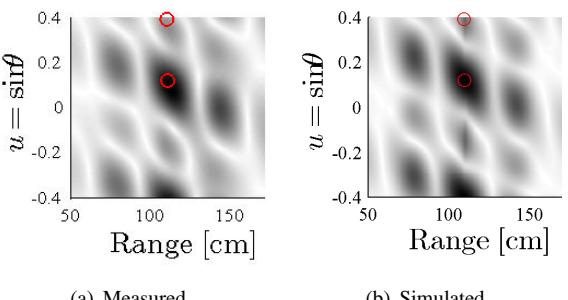
Fig. 6. Measured (a) and simulated (b) transmit signals for the MC signals $\tilde{Y}_{0,b,n}^{\text{MC}1}$ and $\tilde{Y}_{1,b,n}^{\text{MC}2}$ using the modified signal model. The measured and simulated transmit signals are in fair agreement.



(a) Measured.

(b) Simulated.

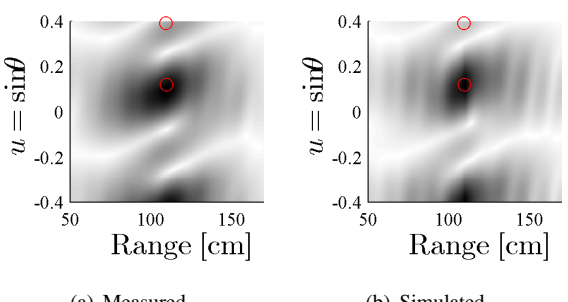
Fig. 7. Measured (a) and simulated (b) transmit signals for the MC signals $\tilde{Y}_{0,b,n}^{\text{SC}1}$ and $\tilde{Y}_{1,b,n}^{\text{SC}2}$ using the modified signal model. The measured and simulated transmit signals are in fair agreement.



(a) Measured.

(b) Simulated.

Fig. 8. Measured (a) and simulated (b) range-angle plots for the MC signals $\tilde{Y}_{0,b,n}^{\text{MC}1}$ and $\tilde{Y}_{1,b,n}^{\text{MC}2}$ using the modified signal model. The target locations are marked on the plots with circles. The measured and simulated range-angle plots are in fair agreement.



(a) Measured.

(b) Simulated.

Fig. 9. Measured (a) and simulated (b) range-angle plots for the SC signal $\tilde{Y}_{0,b,n}^{\text{SC}1}$ and the LFM signal $\tilde{Y}_{1,b,n}^{\text{LFM}1}$ using the modified signal model. The target locations are marked on the plots with circles. The measured and simulated range-angle plots are in fair agreement.